Article

First-Order Isostructural Phase Transition Induced by High Pressure in $Fe(IO_3)_3$

Akun Liang, Saqib Rahman, Hajra Saqib, Placida Rodriguez-Hernandez, Alfonso Muñoz, Gwilherm Nénert, Ibraheem Yousef, Catalin Popescu, and Daniel Errandonea*

HPSTAR
1027-2020

ACCESS | Metrics & More | Article Recommendations

ABSTRACT: The high-pressure (HP) behavior of $Fe(IO_3)_3$ was studied up to 35 GPa using powder X-ray diffraction, infrared micro-spectroscopy, and *ab initio* density-functional theory calculations. $Fe(IO_3)_3$ shows a pressure-induced structural phase transition at 15−22 GPa. Powder X-ray diffraction was employed to obtain the structure of the HP phase. This phase can be described by the same space group ($P6_3$) as the low-pressure phase but with a substantial different c/a ratio. This conclusion is supported by our computational simulations. The discovered phase transition involves a large volume collapse and a change in the coordination polyhedron of iodine, being a first-order transition. It also produces substantial changes in the infrared and Raman vibrational spectra. The pressure dependences of infrared and Raman phonon frequencies and unit-cell parameters have been obtained. A mode assignment is proposed for phonons based upon *ab initio* calculations. The bulk modulus of the two phases was obtained by fitting a Birch−Murnaghan equation of state to synchrotron X-ray powder diffraction data resulting in $B_0 = 55(2)$ GPa for the low-pressure phase and $B_0 = 73(9)$ GPa for the HP phase. Calculations gave $B_0 = 36(1)$ GPa and $B_0 = 48(3)$ GPa for the same phases, respectively. The results are compared with other iodates, in particular $LiIO_3$, for which we have also performed density-functional theory calculations. A possible mechanism driving the observed phase transition will be discussed.

Pressure-induced phase transition in $Fe(IO_3)_3$

Low-pressure structure → Pressure → High-pressure structure
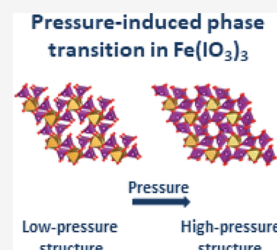
INTRODUCTION

The family of metal iodates has been extensively studied at ambient pressure because of their dielectric, magnetic, or nonlinear optical properties.[1] Many of them have been also studied for the reason that they are superionic conductors.[2] Such properties make them excellent barocaloric materials, very promising for the development of ecofriendly solid-state cooling technologies.[3] On the other hand, numerous iodates are fascinating because they have IO_3 units with lone-pair orbitals,[4] which give materials particular characteristics.[5]

High-pressure (HP) research is known to be an efficient tool to determine the characteristics of materials.[6] In general, HP reduces the interatomic distances in materials in a controlled manner, which results in significant changes of the physical and chemical characteristics.[6] The discoveries in HP research include multiple structural phase transitions which trigger interesting phenomena like metallization or superconductivity.[6,7] Among iodates, only $LiIO_3$,[8−10] KIO_3,[11] and $AgIO_3$[12] have been studied under compression. In a first study on $LiIO_3$,[8] it was proposed that a HP phase would exist beyond 4 GPa. In a subsequent work, it has been found that no phase transition takes place up to 23 GPa.[9] More recently, studies have been extended up to 73 GPa, but no new phase of $LiIO_3$ has been found.[10] In contrast, KIO_3 shows a very different behavior, with phase transitions around 7 and 14 GPa.[11] On the other hand, in $AgIO_3$[12] a new phase was obtained at 2.7 GPa by heating above 240 °C. These facts suggest that the HP

behavior of metal iodates can be extremely complex and should be further studied for a better understanding of the HP behavior of this family of compounds.

In this work, we will study $Fe(IO_3)_3$. The interest on this compound comes not only from the facts described above, but also from the circumstance that its crystal structure (shown in Figure 1) contains zeolitic-like channels, which could lead to an interesting HP behavior.[13] The crystal structure of $Fe(IO_3)_3$ is described by space group $P6_3$.[14] It consists of FeO_6 octahedral units connected by iodine atoms, each of which is coordinated by three oxygen atoms in a trigonal pyramidal geometry with nonbonding lone-pair orbitals (see Figure 1).[14] Such a characteristic makes the HP behavior of compounds interesting and unpredictable.[15] In addition, the crystal structure of $Fe(IO_3)_3$ is isomorphic to the structure of $Cr(IO_3)_3$, $Sc(IO_3)_3$, and other iodates.[16] This makes the results obtained from $Fe(IO_3)_3$ useful to make predictions on the HP behavior of other iodates.

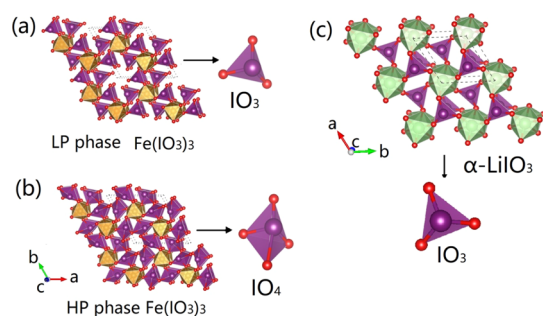In order to characterize the HP behavior of $Fe(IO_3)_3$, we performed synchrotron powder X-ray diffraction (XRD) and
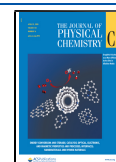
Figure 1. Crystal structure of low-pressure and HP structures of $Fe(IO_3)_3$. Both described by space group $P6_3$. FeO_6 octahedra are shown in yellow and the coordination polyhedra of I atoms in purple. There is a coordination change at the phase transition. The zeolitic channels along the c-axis can be identified in the figure. The crystal structure of $LiIO_3$ is also shown. In this case, LiO_6 octahedra are shown in green.

Fourier transform infrared (FTIR) microspectroscopy measurements, which have been combined with density-functional theory (DFT) calculations. This is the first time that these techniques are used combined to study the HP behavior of an iodate. In the next section, we will provide technical details of our studies and report evidence of the existence of a first-order isostructural phase transition, which triggers a coordination change of iodine atoms and substantial changes in phonons. The behavior of $Fe(IO_3)_3$ will be discussed in comparison with the behavior of other iodates under compression.

■ METHODS

Sample Preparation. The $Fe(IO_3)_3$ sample was prepared by reacting $Fe(NO_3)_3 \cdot 9H_2O$ with $NaIO_3$. An excess of $Fe(NO_3)_3 \cdot 9H_2O$ was used to insure the displacement of the reaction equilibrium. A solution containing $NaIO_3$ was heated up at 60 °C with stirring and a solution of $Fe(NO_3)_3 \cdot 9H_2O$ was added step by step. Then, the solution was allowed to mature for 2 days at 60 °C still under vigorous stirring. The precipitate was recovered by filtration and was dried overnight at 120 °C. Characterization of the as-prepared sample was done by powder XRD using an Empyrean diffractometer from Malvern Panalytical, equipped with a Bragg−Brentano^{HD} setting, using cobalt radiation (λ = 1.789007 Å), and a Bragg−Brentano geometry. A Rietveld refinement was carried

out using the HighScore suite.[17] The XRD pattern of $Fe(IO_3)_3$ and final Rietveld refinement, assuming the crystal structure reported in the literature[14] (space group c), are shown in Figure 2. The matching of the refinement to the experiment is very good. The derived unit-cell parameters are a = 9.2476(4) Å and c = 5.2326(2) Å and the atomic coordinates are reported in Table 1. They agree with the literature.[14] No impurities or minor phases were detected by XRD.

Table 1. Comparison of the Calculated Crystal Structure (Space Group $P6_3$) at Ambient Pressure With Our and Previous Experiments[a]

this work (exp)		a = 9.2476(4) Å		c = 5.2326(2) Å
ref 14		a = 9.19 Å		c = 5.22 Å
ref 1		a = 9.2318(8) Å		c = 5.2297(5) Å
this work (DFT)		a = 9.18767 Å		c = 5.116 Å

atom		x	y	z
Fe(2b)	this work (exp)	0.3333	0.6667	0.625(1)
	ref 14	0.3333	0.6667	0.6387(32)
	ref 1	0.3333	0.6667	0.628(3)
	this work (DFT)	0.3333	0.6667	0.61799
I (6c)	this work (exp)	0.3166(1)	0.9790(3)	0.008(1)
	ref 14	0.3128(3)	0.9779(3)	0
	ref 1	0.3151(2)	0.9782(2)	0.008(2)
	this work (DFT)	0.31703	0.97579	0.00755
O1(6c)	this work (exp)	0.833(2)	0.074(2)	0.223(3)
	ref 14	0.8240(35)	0.0435(34)	0.2414(81)
	ref 1	0.842(2)	0.057(2)	0.241(4)
	this work (DFT)	0.84206	0.07016	0.26332
O2(6c)	this work (exp)	0.589(2)	0.136(2)	0.348(3)
	ref 14	0.5785(39)	0.1266(36)	0.3444(85)
	ref 1	0.583(2)	0.128(2)	0.351(4)
	this work (DFT)	0.57323	0.1251	0.33887
O3(6c)	this work (exp)	0.199(2)	0.717(2)	0.386(2)
	ref 14	0.1967(36)	0.7156(38)	0.3994(64)
	ref 1	0.194(2)	0.712(2)	0.393(3)
	this work (DFT)	0.18927	0.71706	0.3866

^{a}The table includes the unit-cell parameters and atomic coordinates of $Fe(IO_3)_3$ as derived from the Rietveld refinement.

HP X-ray Diffraction. HP angle-dispersive powder XRD experiments were performed at room-temperature (RT) employing a diamond-anvil cell (DAC). As metal iodates can
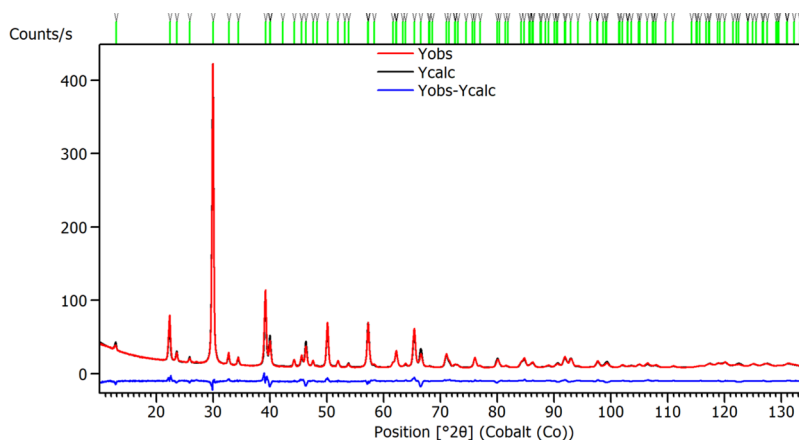
Figure 2. Rietveld refinement of $Fe(IO_3)_3$ corresponding to ambient pressure with statistics R_{wp} = 4.1 (space group $P6_3$, cell parameters a = 9.2476(4) Å and c = 5.2326(2) Å). Ticks indicate the positions of reflections.

be hydrated, in order to avoid the influence of water absorption in the HP behavior,[18] silicone oil was used as the pressure-transmitting medium (PTM),[19] which is quasi-hydrostatic up to 12 GPa, but has been used previously as a pressure medium up to 64 GPa.[20] Beyond 20 GPa, silicone oil is in fact superior to other PTM-like alcohol mixtures.[19] The ruby fluorescence method was employed for pressure calibration.[21] The accuracy of pressure measurements was 0.05 GPa. The experiments were performed at the Shanghai Synchrotron Radiation Facility (SSRF, BL15U1 beamline) using an X-ray wavelength of 0.6199 Å. Two-dimensional (2D) XRD images were collected with a MAR 165 detector. The 2D images were integrated using the Dioptas software.[22] The structural analysis was carried out using PowderCell[23] and FULLPROF.[24]

HP Infrared Spectroscopy. HP FTIR microspectroscopy measurements were performed at MIRAS beamline of the ALBA synchrotron light source. The sample was loaded in a DAC equipped with IIAC-diamonds. In these experiments, CsI[25] was used as the PTM because of its transparency in the Far-IR frequency domain and the ruby scale was used for pressure determination (0.05 GPa accuracy).[21] Synchrotron-based FTIR-microspectroscopy data were recorded in the transmission mode of operation using a masking aperture size of 50 μm × 50 μm. The beam current inside the synchrotron ring was 250 mA. The measurements were performed using a 3000 Hyperion microscope coupled to a Vertex 70 spectrometer (Bruker Optik GmbH, Germ/any). The microscope was equipped with a helium-cooled bolometer detector optimized for operation in a range covering the far-infrared spectral region. A Mylar beam splitter was used in the spectrometer. Spectra were collected using a 15× Schwarzschild magnification objective coupled to a 15× Schwarzschild magnification condenser. Single-point measurements at each pressure value were collected using OPUS 7.5 (Bruker Optik GmbH, Germany) in the 660−100 cm^{-1} Far-IR range with a 4 cm^{-1} spectral resolution and 256 co-added scans per spectrum. The analysis of FTIR results was performed using PeakFit. The background was subtracted using the automatic baseline feature and the peaks were fitted using Gaussian functions. Within the experimental resolution, this treatment should not influence the peak positions.

DFT Calculations. Calculations of the total energy were performed within the framework of the DFT[26] and the projector-augmented wave[27,28] method as implemented in the Vienna ab initio simulations package (VASP).[29−32] A plane-wave energy cutoff of 530 eV was used to ensure a high precision in our calculations. The exchange−correlation energy was described within the generalized gradient approximation (GGA) in the GGA + U method with the Perdew−Burke−Ernzerhof for solids (PBEsol).[33] The GGA + U was used to account for the strong correlation between the electrons in the d shell, on the basis of Dudarev's method.[34] In this method, the Coulomb interaction U and the onsite exchange interaction J^{H} are treated together as an U_{eff}. For our calculations, we employed U_{eff} = 5.4 eV. Similar values were previously used with success in the study of other iron compounds.[35−37] To ensure the quality of the chosen U_{eff} value, we calculated the dependence of the phase transition as a function of the U_{eff} in a range from 3 to 7 eV. The Monkhorst−Pack scheme[38] was employed to discretize the Brillouin zone (BZ) integrations with suitable meshes.

This procedure achieves very high convergences of 1 meV per formula unit in the total energy. In the optimized configurations, the forces are lower than 2 meV/Å per atom in each of the Cartesian directions and the deviation of the stress tensor from a diagonal hydrostatic form is less than 1 kbar. All the structural parameters were obtained at selected optimized volumes.

To study the Raman and infrared phonons, lattice-dynamics calculations were performed at the zone center (Γ point) of the BZ using the direct method.[39] The frequencies of the normal modes are provided by the diagonalization of the dynamical matrix. These calculations also allow us to identify the symmetry and eigenvectors of the phonon modes at the Γ point.

■ RESULTS AND DISCUSSION

HP Phase Transition. Before discussing the HP results, we will comment on the description of the crystal structure at
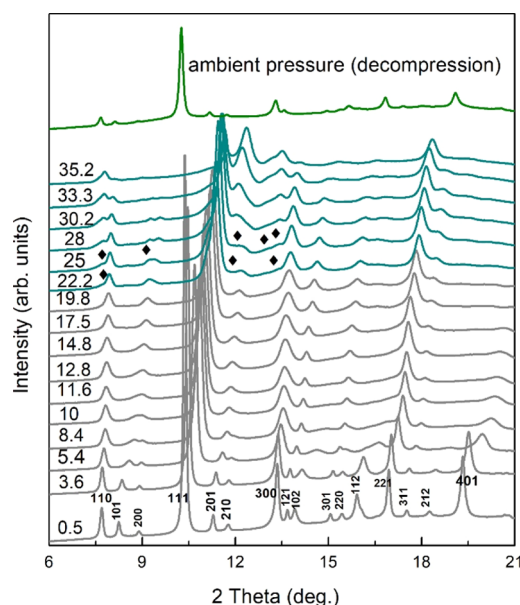
Figure 3. Selection of XRD patterns measured at different pressures, which are indicated in GPa in the figure. Black diamonds indicate the appearance of peaks of the HP phase.

ambient pressure (described by space group $P6_3$) obtained from our DFT calculations. The optimized unit-cell parameters are shown in Table 1 together with the calculated atomic positions. It can be seen that there is a close agreement of calculations with the experimental results, both for lattice parameters and atomic positions. The calculations give a good description of the crystal structure, underestimating the unit-cell volume by only 3%. Such a small difference is typical of DFT calculations being caused by an underestimation of the cohesion energy.[40,41]

We will start now discussing the HP results. A selection of XRD patterns measured under pressure are summarized in Figure 3. At the lowest pressure measured in the DAC (0.5 GPa), the XRD pattern corresponds to the known-crystal structure of Fe(IO$_3$)$_3$ (space group $P6_3$). This is confirmed by structural refinements. The results of the refinements are shown in Figure 4. Under compression, up to 19.8 GPa, the changes in the XRD patterns are limited to the shift of peaks toward higher angles because of the contraction of the unit cell.
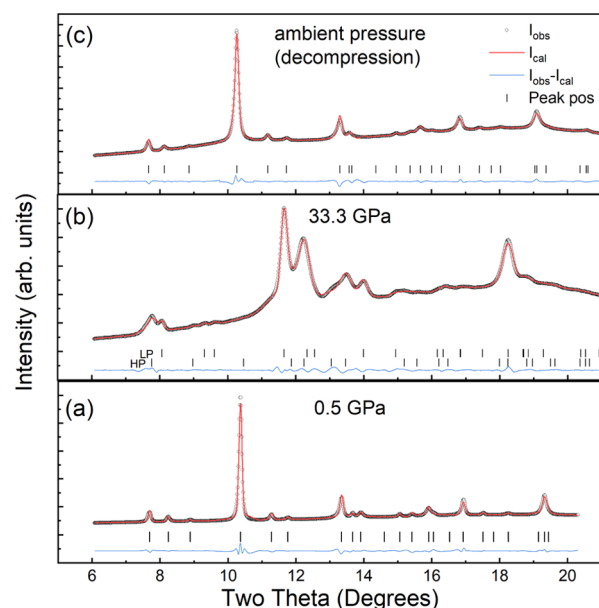
Figure 4. Typical refinements of XRD patterns measured for the low-pressure and HP phases (both described to space group $P6_3$) with the Rietveld method. The pressures are indicated in GPa in the figure. At 33 GPa, the phase coexistence can be seen.

**Table 2. Calculated Crystal Structure of the LP Phase ($P6_3$) at 11.6 GPa and HP Phase ($P6_3$) at 22 GPa[a]**

low-pressure phase		
a = 9.072 Å, c = 4.293 Å (DFT at 11.6 GPa)		
a = 9.067(2) Å, c = 4.659(1) Å (XRD at 11.6 GPa)		
atom	x	y	z
Fe (2b)	0.3333	0.6667	0.6391
I (6c)	0.3148	0.9930	0.0484
O1 (6c)	0.8284	0.0433	0.2179
O2 (6c)	0.5779	0.1166	0.3583
O3 (6c)	0.1965	0.7240	0.3648
high-pressure phase		
a = 9.276 Å, c = 3.570 Å (DFT at 22 GPa)		
a = 9.159(2) Å, c = 3.959(1) Å (XRD at 22.2 GPa)		
atom	x	y	z
Fe (2b)	0.3333	0.6667	0.5702
I (6c)	0.3171	−0.0124	0.1335
O1 (6c)	0.8481	0.0658	0.2775
O2 (6c)	0.6012	0.1194	0.3004
O3 (6c)	0.1772	0.7239	0.3009

[a]Experimental unit-cell parameters are also shown.

All the patterns up to 19.8 GPa can be explained by the ambient-pressure crystal structure with the corresponding change of unit-cell parameters. At 22.2 GPa, additional peaks (denoted by black diamonds in Figure 3) can be seen in the XRD patterns. These peaks gradually grow in intensity as the pressure increases at the same time that more additional peaks become evident. In parallel, the peaks assigned to the ambient-pressure phase become weaker. All these facts indicate the occurrence of a phase transition, which is also supported by our FTIR experiments, which detected the transition at 15 GPa and by DFT calculations. Our computing simulations found at 12 GPa, during the optimization of the crystal structure, that the structure of $Fe(IO_3)_3$ "spontaneously" suffers an abrupt change of the c/a axial ratio and a volume collapse of nearly
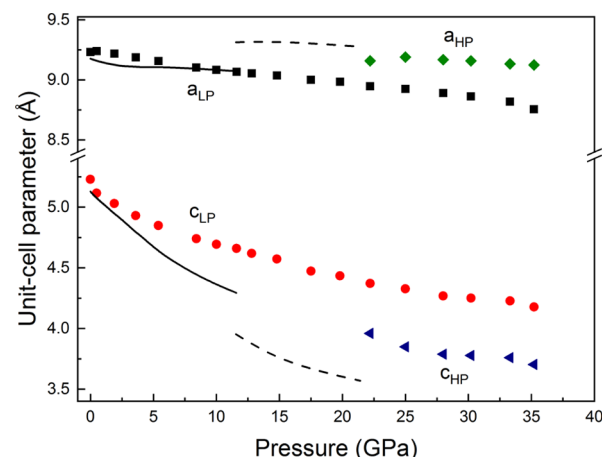
Figure 5. Pressure dependence of unit-cell parameters. Lines are from calculations and symbols from experiments. Experimental errors are smaller than the symbol size.
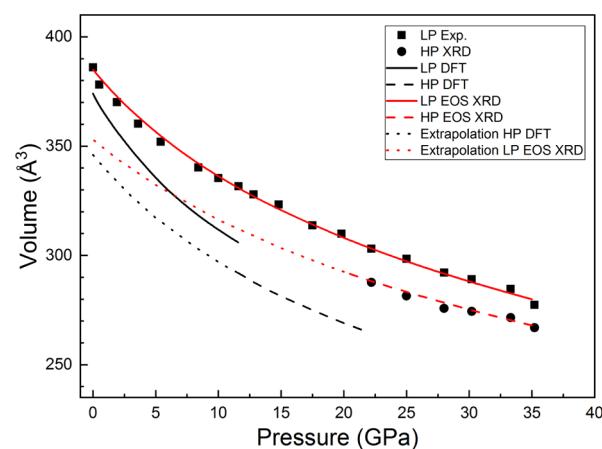
Figure 6. Pressure dependence of unit-cell volume. Black lines are from calculations and symbols from experiments. The red lines represent the EOS fits using the Birch–Murnaghan EOS described in the text. The dotted lines are the extrapolations to ambient pressure of the results of the HP phase. Experimental errors are smaller than the symbol size.

5% when compared with the low-pressure phase at the same pressure. This "spontaneous" evolution of the crystal structure could be interpreted as the occurrence of an isostructural phase transition to a HP phase, which is described by the same space group, $P6_3$, than the low-pressure phase. The new phase remains stable up to the highest pressure achieved in our studies. The structural information of the HP phase is given in Table 2. In this table, we also include structural information of the low-pressure phase at 11.6 GPa. Comparing the results at ambient pressure, with those of the low-pressure phase at 11.6 GPa and the HP phase at 22 GPa, it can be seen that pressure modifies not only the unit-cell parameters but also the atomic positions. All of them change gradually in the low-pressure phase, but the structural parameters undergo a discontinuous change at the phase transition.

The structural change found by calculations is related to the formation of a fourth I−O bond, modifying the iodine coordination polyhedron from the common trigonal pyramidal geometry to a tetrahedral-like geometry (see Figure 1). We made this conclusion based upon changes of bond distances. Such a coordination change could be triggered by pressure,

Table 3. Equation of State Parameters for Different Iodates

phase	BM-EOS	V_0 (Å³)	B_0 (GPa)	B_0'	reference
		$Fe(IO_3)_3$			
LP	Exp 3rd-order	385	55(2)	4.3(0.3)	this work
LP	Theo 3rd-order	374	36(1)	4.6(0.1)	
HP	Exp 2nd-order	353(9)	73(9)	4.0	
HP	Theo 2nd-order	346(5)	48(3)	4.0	

phase	BM-EOS	V_0 (Å³)	B_0 (GPa)	B_0'	reference
		$LiIO_3$			
α	Theo 3rd-order	134.4	34(1)	4.2(0.2)	this work
α	Exp 3rd-order	134.5	34(3)	5(0.8)	9
α	Exp 3rd-order	134.5	55(3)	2.9(0.4)	10

phase	BM-EOS	V_0 (Å³)	B_0 (GPa)	B_0'	reference
		KIO_3			
ambient pressure phase (triclinic phase III)	Exp 2nd-order	355.3	24.3(5)	4.0	11
high pressure phase I (HP I)	Exp 2nd-order	152.3(4)	67(3)	4.0	
HP I	DFT 2nd-order	150.81	70.9	4.0	
HP I	DFT 3rd-order	150.81	67.9	5.9	

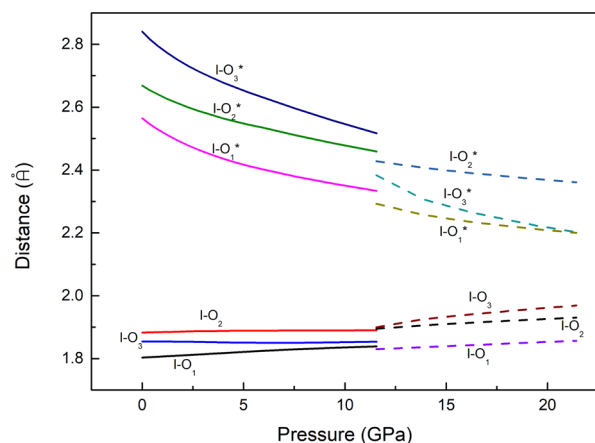| phase		V_0 (Å³)	B_0 (GPa)	reference
		$LiZn(IO_3)_3$		
ambient pressure phase	estimated from empirical relations	527.04	55	52

Figure 7. Pressure dependence of I−O bond distances obtained from calculations.
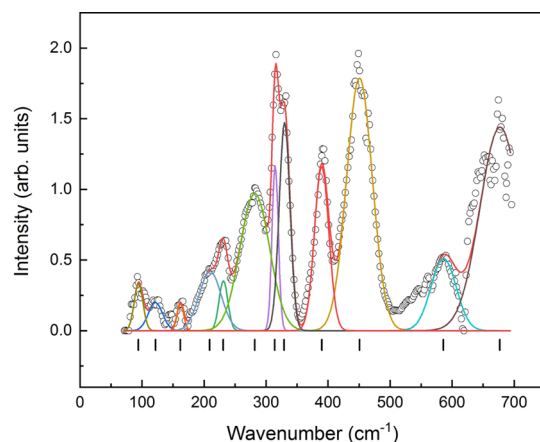

Figure 8. Background-subtracted IR spectrum at ambient conditions. The Gaussians used for the fits are also shown.

which favors the linking of the lone electron pair of iodine to one oxygen atom in the nearest IO_3 unit. A confirmation of it could come from future HP extended X-ray absorption fine-structure measurements at the iodine K-edge. The proposed coordination change of iodine would cause a closure of the zeolitic channels of $Fe(IO_3)_3$, see Figure 1. The relative decrease of the empty volume is estimated to be 4%. As we will show below, this structural modification has consequences in the lattice vibrations of $Fe(IO_3)_3$.

A Rietveld analysis[42] of the XRD patterns measured from 22.2 GPa up to 35.2 GPa confirms the theoretical predictions. These patterns can be explained by the coexistence of the low-pressure and HP phases, both phases described by space group $P6_3$. This can be seen in Figure 4 where we show the fitting of the XRD pattern measured at 33.3 GPa considering both phases. By comparing the intensities of the main peaks assigned to each phase, we quantified the fraction of each of them, increasing the fraction of the HP phase from 5% at 22.2 GPa to 66% at 35.2 GPa. We also observed that the phase transition is reversible as shown by the XRD patterns measured after decompression (see Figures 3 and 4). Upon decompression, we did not collect intermediate points from the highest pressure to ambient pressure; thus, we cannot discuss if there is hysteresis or not in the transition. Phase coexistence has been observed in many other oxides under HP.[43,44] The reasons for it could be multiple. An argument recently proposed to explain it is the presence of kinetic barriers, which could be locally overcome by the presence of defects which provide a kinetic pathway of the phase transition.[45]

The difference between the transition pressure predicted by DFT and the experimental onset of the phase transition can be because calculations have been performed at 0 K temperature.[46] However, it can be also related to the presence of kinetic barriers.[49] These facts, and the possible presence of radial pressure gradients,[47] can be the cause of the observed phase coexistence. On the other hand, the fact that the transition pressure is lower in FTIR experiments than in XRD experiments could be related to the influence in experiments of nonhydrostatic stresses in FTIR experiments because of the use of a solid pressure medium, where nonhydrostaticity is even larger than in silicone oil.[48,49] A systematic analysis of the influence of nonhydrostaticity and kinetic barriers in the HP behavior of $Fe(IO_3)_3$ is beyond the scope of this work.

Table 4. Frequency of Phonons (ω), Pressure Coefficient ($d\omega/dP$), and Grüneisen Parameters for Different Modes (γ) of the Low-Pressure Phase[a]

| mode	theory (ambient pressure, B_0 = 36 GPa)			experiment (ambient pressure, B_0 = 55 GPa)				
	ω (cm^{-1})	$d\omega/dP$ (cm^{-1}/GPa)	γ	ω^{55} (cm^{-1})	ω^{56} (cm^{-1})	ω (cm^{-1}) (this work)	$d\omega/dP$ (cm^{-1}/GPa)	γ
A	57.3	0.73	0.46		55(R)			
E1	65.6	2.07	1.13					
E2	79.8	1.46	0.66					
E2	89.6	3.30	1.32	86(R)	85(R)			
A	112.3	1.85	0.59		110(R)	94(2) (IR)		
E1	119.8	1.65	0.50					
A	126.1	1.92	0.55	127(IR), 125(R)	125(R)	122(2) (IR)		
E2	131.8	3.11	0.85					
E1	165.4	4.72	1.03	168(IR), 166(R)	165(R)	162(2) (IR)	5.25(1)	1.78(1)
E2	172.3	4.66	0.97					
E2	194.5	4.75	0.88					
E1	202.2	4.78	0.85		205(R)			
A	212.7	4.35	0.74			209(2) (IR)	2.80(1)	0.74(1)
E1	219.4	4.68	0.77					
E2	223.4	5.80	0.94	223(R)	225(R)			
A	239.8	4.56	0.69	228(IR)		231(2) (IR)	4.00(1)	0.95(1)
E2	245.3	6.02	0.88					
E1	269.8	3.82	0.51	266(R)	265(R)			
A	270.7	4.27	0.57					
A	291.7	4.35	0.54			282(2) (IR)	2.43(1)	0.47(1)
E1	316.5	4.60	0.52	314(IR), 320(R)	315(R)	314(2) (IR)	0.62(1)	0.11(1)
E2	334.2	2.95	0.32	350(R)	350(R)			
E1	382.5	3.68	0.35			329(2) (IR)	3.15(1)	0.53(1)
E2	385.5	3.82	0.36					
A	391.4	4.37	0.40	395(IR), 394(R)	395(R)	390(2) (IR)	3.64(1)	0.51(1)
A	436.9	5.12	0.42					
E2	445.1	5.10	0.41					
E1	445.9	5.79	0.47	451(IR), 450(R)	445(R)	451(2) (IR)	5.82(1)	0.71(1)
E2	619.8	1.02	0.06					
E1	622.1	1.36	0.08			586(2) (IR)	2.05(1)	0.19(1)
A	637.7	−0.01	0.00					
E2	674.7	−0.17	−0.01					
E1	697.9	−2.26	−0.12	699(IR), 685(R)	685(R)	677(2) (IR)		
A	729.2	−3.29	−0.16	726(R)	726(R)			
E1	770.7	−2.24	−0.10	764(IR), 755(R)	756(R)			
A	773.6	−1.37	−0.06					
E2	791.1	−3.08	−0.14		796(R)			

[a] A and E$_1$ modes are Raman- and IR-active. E$_2$ modes are only Raman-active. In the results from the literature, R and IR means the experimental technique (Raman or IR).

Compressibility. From our XRD experiments and calculations, we have obtained the pressure dependence of the unit-cell parameters of both phases of Fe(IO$_3$)$_3$. The results are shown in Figure 5. Both methods agree in the fact that the crystal structure is significantly more compressible along the c-axis than along the a-axis. Such anisotropic behavior is similar to that of other members of this family of compounds.[10,11] This is related to the fact that IO$_3$ units are oriented in such a way that the lone-pair electrons of iodine are basically aligned along the c-axis. In Figure 5, the abrupt change of the unit-cell parameters at the phase transition can be also seen.

In Figure 6, we present the pressure evolution of the unit-cell volume. We found that Fe(IO$_3$)$_3$ is highly compressible, with a 22% volume reduction from ambient pressure to the transition pressure (22 GPa). We also found that, the pressure dependence of the volume can be described using the 2nd and 3rd Birch–Murnaghan equations of state (EOS),[30] for the HP

and low-pressure phases, respectively. The fits have been carried out using the EOSFit programme.[51] The values of the determined ambient pressure unit-cell volume (V_0), bulk modulus (B_0), and pressure derivative (B_0') for the different phases are given in Table 3. These parameters are compared there with those previously reported for other iodates. The low-pressure phase has a bulk modulus of 55(2) and 36(1) GPa according to experiments and calculations, respectively. These values lie within the range of values reported in the literature for the bulk modulus of LiIO$_3$[9,10] and LiZn(IO$_3$)$_3$,[52] but are larger than the bulk modulus of KIO$_3$ (see Table 3).[11] Regarding the HP phase, it can be seen that after the phase transition the bulk modulus is considerably enlarged (i.e., compressibility is reduced) as reported also in KIO$_3$.[11] This is mainly due to the collapse of the volume at the phase transition (see Figure 6). The abrupt change of the volume ($\Delta V/V = -5.5\%$) and the axial ratio at the phase transition and the enhancement of the bulk modulus support that the phase
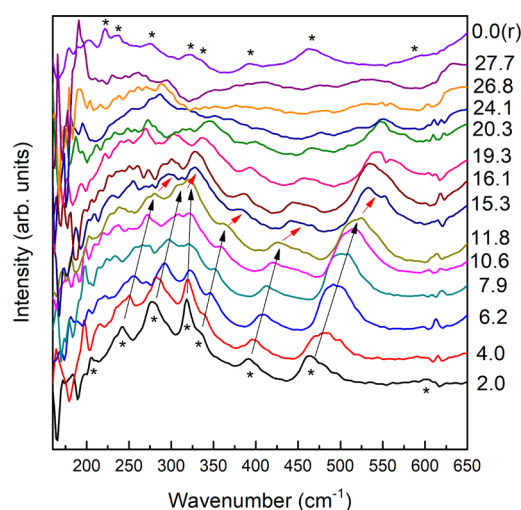
Figure 9. IR spectra at different pressures which are indicated in GPa in the figure. The asterisks indicate the different phonon. Black arrows show the pressure evolution in the low-pressure phase. Red arrows show the changes at the phase transition. The upper trace shows the spectrum measured at ambient pressure after pressure release, which is denoted by (*r*).
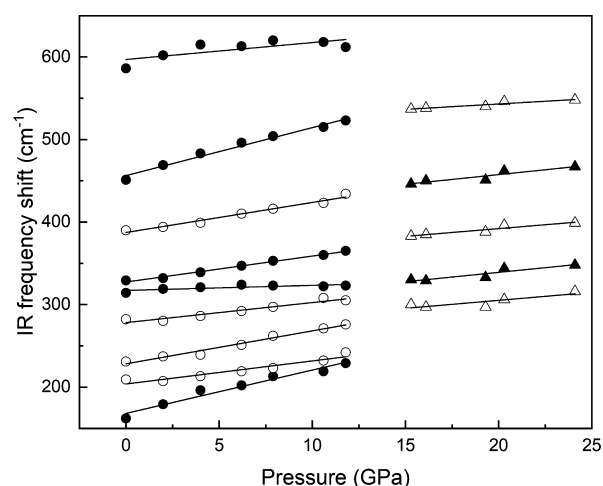
Figure 10. Pressure dependence of IR modes obtained from experiments. Circles: low-pressure phase. Triangles: HP phase. Black and white colors are used for E_1 and A modes, respectively. Experimental errors are smaller than the symbol size.

transition is of a first-order nature.[53] This is also supported by the sluggish character of the transition, the observed coexistence of phases, and the proposed existence of kinetic barriers, and formation of new I−O bonds. To conclude the discussion on the bulk modulus, we would like to mention that given the discrepancies found in the literature on the bulk modulus of $LiIO_3$,[9,10] we have calculated the pressure dependence of the volume of this compound. The determined EOS is shown in Table 3. Our results agree better with the results reported by Hu[9] as compared to the results reported by Zhang.[10]

Polyhedral Changes. A deeper understanding of the HP behavior can be obtained from the analysis of the polyhedral behavior.[54] As calculations and experiments give a similar description of the pressure evolution of unit-cell parameters, and oxygen positions cannot be accurately determined from our HP XRD experiments, we will base this part of the

discussion on the *ab initio* calculations. The first thing we have noticed is that in the low-pressure phase, the FeO_6 octahedron becomes gradually more symmetric under compression, being in fact a regular octahedron just before the phase transition. If the pressure dependence of the volume of this octahedron is described with a 2nd order Birch−Murnaghan EOS, a bulk modulus of 115(5) GPa is obtained for it. Thus, the volume reduction of FeO_6 cannot account for the volume decrease of the crystal, which is in part determined by the reduction of the "empty" space surrounding the IO_3 units. As a consequence, the second-coordination sphere of iodine atoms is reduced favoring the formation of new I−O bonds. This can be seen by looking at the pressure dependence of I−O bonds in Figure 7. In this figure, it can be observed that the I−O distances of the trigonal pyramidal IO_3 unit (lines without asterisks in the figure) are little affected by pressure, with a tendency to the increase of the average bond distances. In contrast, the next three nearest oxygen atoms get closer to iodine upon pressure increase (lines with asterisks in the figure). On the other hand, at the phase transition there is an abrupt change of the I−O distances. In particular, if distances below 2.4 Å are considered, the coordination number of iodine atoms becomes four as commented before (shown in Figure 1). In addition, there are two additional oxygen atoms, which were in the low-pressure phase on the side of the lone-pair electrons of iodine, which also get closer to the iodine atoms. This phenomenon is enhanced under further compression, the coordination becoming around iodine fivefold at the highest pressure, with the sixth nearest oxygen at a distance of 2.4 Å, which is shorter than the fourth I−O distance at ambient pressure.

IR and Raman Phonons. To conclude, we will discuss the vibrational properties of $Fe(IO_3)_3$. We will start this section commenting on the IR and Raman spectra at low pressure. Figure 8 shows the IR absorption spectrum measured at ambient conditions outside the DAC. We identified at least 12 absorption bands. Their frequencies have been determined making a Gaussian fit to the different bands (see Figure 8). The frequencies of six of the modes agree well with the IR modes reported in the literature.[55] In order to assign the modes and discuss the infrared results, we used our DFT calculations. According to group theory, $Fe(IO_3)_3$ has 24 IR-active modes ($12\,A + 12 \times 10^1$). These modes are also Raman-active. There are, in addition, 12 extra Raman modes with symmetry E_2, making a total of are 37 Raman-active modes ($12\,A + 12 \times 10^1 + 13 \times 10^2$). From our DFT simulations, we have calculated the frequencies of all the vibrational modes, which are shown in Table 4. The calculated frequencies agree reasonably well with the present and previous IR and Raman experiments.[56,57] Differences between calculated and experimental mode frequencies are similar to the difference between different experimental studies (see Table 4). The mode assignment given by calculations is also reported in the table. It has been noticed that there is a group of phonons with frequencies lower than 330 cm^{-1}, another group with frequencies between 360 and 425 cm^{-1}, and a third group with frequencies higher than 590 cm^{-1}. The high-frequency modes correspond to stretching modes within the pyramidal IO_3 unit, the intermediate-frequency modes correspond to bending vibration of IO_3, and the low-frequency modes can be basically associated to vibrations that involve the movement of Fe atoms and the IO_3 units as a rigid element.

The results of HP FTIR measurements are shown in Figure 9. The spectrum at 2 GPa resembles the ambient pressure

Table 5. Frequency of Phonons (ω), Pressure Coefficient (dω/dP), and Grüneisen Parameters for Different Modes (γ) of the HP Phase at 15.3 GPa[a]

| mode	theory (15 GPa, B_0 = 48 GPa)			experiment (15.3 GPa, B_0 = 73 GPa)		
	ω (cm^{-1})	dω/dP (cm^{-1}/GPa)	γ	ω (cm^{-1}) (this work)	dω/dP (cm^{-1}/GPa)	γ
A	87.8	0.19	0.10			
E2	99.3	0.83	0.40			
E1	127.0	0.20	0.08			
E2	138.0	0.28	0.10			
E1	144.8	0.07	0.02			
A	150.9	0.64	0.20			
A	186.2	1.71	0.44			
E2	199.9	1.95	0.47			
A	226.4	0.48	0.10			
E1	231.0	2.85	0.59			
E2	243.9	2.85	0.56			
E1	267.4	2.39	0.43			
E2	272.0	2.76	0.49			
A	280.9	2.87	0.49			
E2	295.2	2.43	0.40			
E1	311.5	2.12	0.33	300(2) (IR)	1.94(1)	0.47(1)
A	323.8	1.67	0.25			
E1	329.1	3.86	0.56	330(2) (IR)	2.27(1)	0.50(1)
E2	344.6	4.14	0.58			
A	348.7	4.23	0.58			
E1	358.3	4.49	0.60	383(2) (IR)	1.87(1)	0.35(1)
E	403.3	4.22	0.50			
A	432.4	2.76	0.31			
E2	436.6	3.40	0.37			
E1	455.2	3.04	0.32	446(2) (IR)	2.34(1)	0.38(1)
A	468.3	3.81	0.39			
E1	469.7	4.17	0.43			
E2	498.3	3.23	0.31			
A	558.5	0.09	0.01	537(2) (IR)	1.31(1)	0.17(1)
E1	564.2	−0.16	−0.01			
E2	602.9	−1.24	−0.10			
E2	625.9	−0.21	−0.02			
E1	651.8	−1.21	−0.09			
A	678.1	−2.39	−0.17			
A	728.2	−0.95	−0.06			
E1	738.4	−1.39	−0.09			
E2	750.2	−1.88	−0.12			

[a]A and E$_1$ modes are Raman- and IR-active. E$_2$ modes are only Raman-active.

spectrum. In this case, only the modes between 200 and 650 cm^{-1} can be clearly identified. They are indicated by asterisks in Figure 9. In the figure, it can be seen that as pressure increases, up to 11.8 GPa, the only change in the IR spectrum is the gradual shift of the mode frequencies toward higher frequencies (see the black arrows in the figure). This is a consequence of the shortening of interatomic distances. However, at 15.3 GPa drastic changes occur in the IR spectrum, supporting the existence of the phase transition previously described. These changes involve the merging of several modes and an abrupt phonon shift, which is shown by red arrows in the figure. We consider this as an evidence of the phase transition. We will show below that such changes in phonon frequencies are in agreement with changes predicted by DFT calculations. Therefore, the phase transition detected by FTIR spectroscopy can be correlated to the one observed by XRD. In fact, the changes of IR phonons at 15.3 GPa are related to the changes in bond distances previously described.[58] Upon further compression, the modes again

gradually shift with pressure. In addition, there also a loss of intensity because of the decrease of the sample thickness. Under decompression, the changes are reversible as can be seen in the spectrum shown in the top of Figure 9. The pressure dependences of the identified IR modes are shown in Figure 10. There, not only the discontinuity in frequencies but also the changes in the pressure dependence can be seen. In both phases, the modes have a linear pressure dependence. In Tables 4 and 5, we summarize the theoretical and experimental pressure dependence of phonons (including also the Grüneisen parameter) for both the low-pressure phase (at ambient pressure) and the HP phase (at 15.3 GPa).

In Figures 11 and 12, we represent the calculated pressure dependence for IR modes and for the modes that are only Raman-active, respectively. There, it can be seen that the structural changes associated to the phase transition cause drastic changes in the frequencies of the modes. Indeed, they resemble the changes observed in FTIR experiments. This fact supports the assignment of changes in the IR spectrum at 15.3
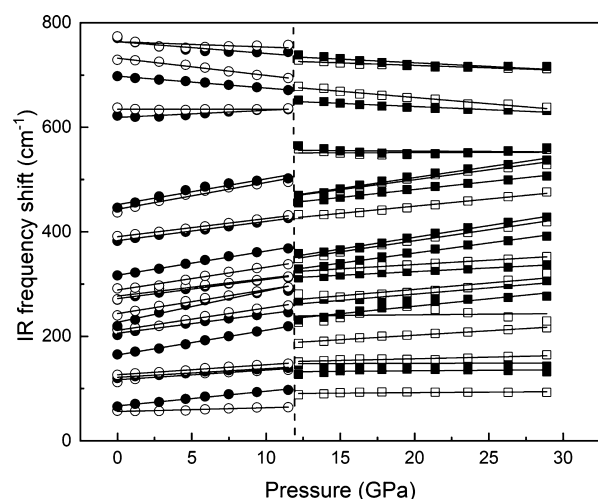
Figure 11. Pressure dependence of A and E_1 modes obtained from calculations. These modes are Raman- and IR-active. Circles: low-pressure phase. Squares: HP phase. Black and white colors are used for E_1 and A modes, respectively.
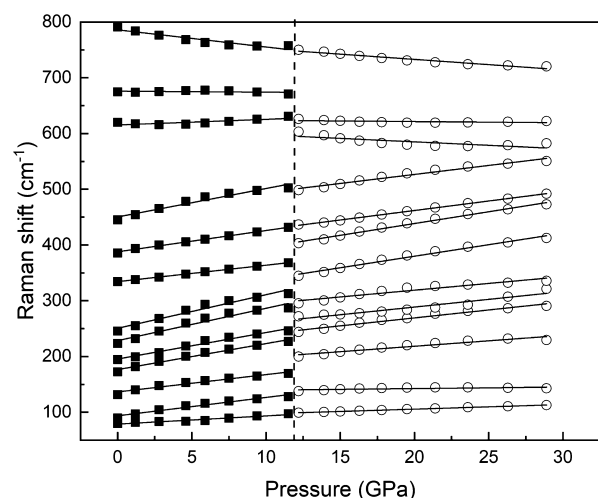
Figure 12. Pressure dependence of E_2 modes obtained from calculations. These modes are only Raman-active. Squares: low-pressure phase. Circles: HP phase.

GPa because of the phase transition predicted by DFT and observed in XRD experiments. Another interesting feature that can be observed in Figures 11 and 12 (and in Tables 4 and 5) is the existence of modes, which are gradually softened under compression. These modes belong to those assigned to the internal vibrations of the iodate molecule. The presence of such soft modes in the low-pressure phase is consistent with the occurrence of a phase transition, as "weak soft-modes" (they are not classical soft-modes because the frequency never reaches zero and therefore their existence does not contradict the first-order nature of the transition) could be related to a collective instability, which tend to make the crystal structure unstable.[58] The presence of similar modes in the HP phase suggests the existence of a second phase transition at pressure beyond those pressures covered by the present study.

CONCLUSIONS

We have studied the HP behavior of $Fe(IO_3)_3$ by means of XRD, infrared micro-spectroscopy, and DFT calculations. This

is the first time an iodate is studied by HP FTIR spectroscopy. We have found evidence of the existence of a pressure-driven phase transition. The HP phase can be described by the same space group as the low-pressure phase; however, the transition is a first-order transformation involving a volume collapse larger than 5%. The phase transition is related to the change of the activity of iodine lone-pair electrons, which under compression prefer to link to oxygen atoms. The pressure dependence of unit-cell parameters for the two phases has been determined. The fit of the pressure−volume results with a Birch−Murnaghan equation of state indicate that $Fe(IO_3)_3$ is highly compressible with a bulk modulus $B_0 = 55(2)$ GPa. The HP phase is less compressible with $B_0 = 73(9)$ GPa. Finally, detailed information is provided on infrared- and Raman-active modes, being the pressure dependence of phonon frequencies determined. Based upon calculations, we have assigned the symmetry of different modes.

AUTHOR INFORMATION

Corresponding Author

Daniel Errandonea − *Departamento de Física Aplicada— ICMUV—MALTA Consolider Team, Universitat de València, 46100 Burjassot (Valencia), Spain;* ◎ orcid.org/0000-0003-0189-4221; Email: daniel.errandonea@uv.es

Authors

Akun Liang − *Departamento de Física Aplicada—ICMUV— MALTA Consolider Team, Universitat de València, 46100 Burjassot (Valencia), Spain*

Saqib Rahman − *Center for High Pressure Science and Technology Advanced Research Shanghai, 201203 Shanghai, China*

Hajra Saqib − *Shanghai Institute of Technical Physics, Chinese Academy of Science, 200083 Shanghai, China*

Placida Rodriguez-Hernandez − *Departamento Física, Malta Consolider Team, and Instituto de Materiales y Nanotecnología, Universidad de La Laguna, 38206 La Laguna, Spain;* ◎ orcid.org/0000-0002-4148-6516

Alfonso Muñoz − *Departamento Física, Malta Consolider Team, and Instituto de Materiales y Nanotecnología, Universidad de La Laguna, 38206 La Laguna, Spain;* ◎ orcid.org/0000-0003-3347-6518

Gwilherm Nénert − *Malvern Panalytical B.V., 7602 EA Almelo, The Netherlands*

Ibraheem Yousef − *CELLS-ALBA Synchrotron Light Facility, 08290 Barcelona, Spain*

Catalin Popescu − *CELLS-ALBA Synchrotron Light Facility, 08290 Barcelona, Spain*

Complete contact information is available at:
https://pubs.acs.org/10.1021/acs.jpcc.0c02080

Notes

The authors declare no competing financial interest.

Competividad through the FIS2017-83295 project. The FTIR experiments were performed at MIRAS beamline at the ALBA Synchrotron with the collaboration of ALBA staff.

■ REFERENCES

(1) Galez, C.; Mugnier, Y.; Bouillot, J.; Lambert, Y.; Le Dantec, R. Synthesis and Characterisation of $Fe(IO_3)_3$ Nanosized Powder. *J. Alloys Compd.* **2006**, *416*, 261−264.

(2) Sorokin, N. I.; Shaldin, Y. V. Thermally Induced Charge Relaxation in α-$LiIO_3$ Superionic Conductor. *Phys. Solid State* **2017**, *59*, 1713−1716.

(3) Sagotra, A. K.; Errandonea, D.; Cazorla, C. Mechanocaloric Effects in Superionic Thin Films from Atomistic Simulations. *Nat. Commun.* **2017**, *8*, 963.

(4) Hermet, P. First-Principles Based Analysis of the Piezoelectric Response in α-$LiIO_3$. *Comput. Mater. Sci.* **2017**, *138*, 199−203.

(5) Gonzalez-Platas, J.; Rodriguez-Hernandez, P.; Muñoz, A.; Rodríguez-Mendoza, U. R.; Nénert, G.; Errandonea, D. A High-Pressure Investigation of the Synthetic Analogue of Chalcomenite, $CuSeO_3 \cdot 2H_2O$. *Crystals* **2019**, *9*, 643.

(6) Mao, H.-K.; Chen, B.; Chen, J.; Li, K.; Lin, J.-F.; Yang, W.; Zheng, H. Recent Advances in High-Pressure Science and Technology. *Matter Radiat. Extremes* **2016**, *1*, 59−75.

(7) Errandonea, D.; Garg, A. B. Recent Progress on the Characterization of the High-Pressure Behaviour of AVO_4 Orthovanadates. *Prog. Mater. Sci.* **2018**, *97*, 123−169.

(8) Liu, J.; Shen, Z.; Zhang, Y.; Yin, X.; He, S. The P-T Phase Diagram of Lithium Iodate $(LiIO_3)$ up to 40 Kbars. *Acta Phys. Sin.* **1983**, *32*, 118−123.

(9) Hu, J.; Chen, L.; Wang, L.; Tang, R.; Che, R. Isothermal Compression of α-$LiIO_3$ and Its Phase Transition under High Pressure and High Temperature. *Acta Phys. Sin.* **1987**, *36*, 1099−1104.

(10) Zhang, W. W.; Cui, Q. L.; Pan, Y. W.; Dong, S. S.; Liu, J.; Zou, G. T. High-Pressure x-Ray Diffraction Study of $LiIO_3$ to 75 GPa. *J. Phys.: Condens. Matter* **2002**, *14*, 10579−10582.

(11) Bayarjargal, L.; Wiehl, L.; Friedrich, A.; Winkler, B.; Juarez-Arellano, E. A.; Morgenroth, W.; Haussühl, E. Phase Transitions in KIO_3. *J. Phys.: Condens. Matter* **2012**, *24*, 325401.

(12) Suffren, Y.; Gautier-Luneau, I.; Darie, C.; Goujon, C.; Legendre, M.; Leynaud, O. First Evidence of a Phase Transition in a High-Pressure Metal Iodate: Structural and Thermal Studies of $AgIO_3$ Polymorphs. *Eur. J. Inorg. Chem.* **2013**, *2013*, 3526−3532.

(13) Jordá, J. L.; Rey, F.; Sastre, G.; Valencia, S.; Palomino, M.; Corma, A.; Segura, A.; Errandonea, D.; Lacomba, R.; Manjón, F. J.; et al. Synthesis of a Novel Zeolite through a Pressure-Induced Reconstructive Phase Transition Process. *Angew. Chem., Int. Ed.* **2013**, *125*, 10652−10656.

(14) Jansen, M. Zur Kistallstruktur von FeJ_3O_9. *J. Solid State Chem.* **1976**, *17*, 1−6.

(15) Pereira, A. L. D. J.; Santamaría-Pérez, D.; Vilaplana, R.; Errandonea, D.; Popescu, C.; Da Silva, E. L.; Sans, J. A.; Rodríguez-Carvajal, J.; Muñoz, A.; Rodríguez-Hernández, P.; et al. Experimental and Theoretical Study of $SbPO_4$ under Compression. *Inorg. Chem.* **2020**, *59*, 287−307.

(16) Phanon, D.; Mosset, A.; Gautier-Luneau, I. New Materials for Infrared Non-Linear Optics. Syntheses, Structurarl Characterisations, Second Harmonic Generation and Optical Transparency of $M(IO_3)_3$ Metallic Iodates. *J. Mater. Chem.* **2007**, *17*, 1123−1130.

(17) Degen, T.; Sadki, M.; Bron, E.; König, U.; Nénert, G. The HighScore suite. *Powder Diffr.* **2014**, *29*, S13−S18.

(18) Bandiello, E.; Errandonea, D.; Ferrari, S.; Pellicer-Porres, J.; Martínez-García, D.; Achary, S. N.; Tyagi, A. K.; Popescu, C. Pressure-Induced Hexagonal to Monoclinic Phase Transition of Partially Hydrated $CePO_4$. *Inorg. Chem.* **2019**, *58*, 4480−4490.

(19) Klotz, S.; Chervin, J.-C.; Munsch, P.; Le Marchand, G. Hydrostatic Limits of 11 Pressure Transmitting Media. *J. Phys. D: Appl. Phys.* **2009**, *42*, 075413.

(20) Shen, Y.; Kumar, R. S.; Pravica, M.; Nicol, M. F. Characteristics of Silicone Fluid as a Pressure Transmitting Medium in Diamond Anvil Cells. *Rev. Sci. Instrum.* **2004**, *75*, 4450−4454.

(21) Mao, H. K.; Xu, J.; Bell, P. M. Calibration of the Ruby Pressure Gauge to 800 Kbar under Quasi-Hydrostatic Conditions. *J. Geophys. Res.* **1986**, *91*, 4673−4676.

(22) Prescher, C.; Prakapenka, V. B. DIOPTAS: A Program for Reduction of Two-Dimensional X-Ray Diffraction Data and Data Exploration. *High Pressure Res.* **2015**, *35*, 223−230.

(23) Kraus, W.; Nolze, G. POWDER CELL - A Program for the Representation and Manipulation of Crystal Structures and Calculation of the Resulting X-Ray Powder Patterns. *J. Appl. Crystallogr.* **1996**, *29*, 301−303.

(24) Rodríguez-Carvajal, J. Recent Advances in Magnetic Structure Determination by Neutron Powder Diffraction. *Phys. B Condens. Matter* **1993**, *192*, 55−69.

(25) Asaumi, K.; Kondo, Y. Effect of Very High Pressure on the Optical Absorption Spectra in CsI. *Solid State Commun.* **1981**, *40*, 715−718.

(26) Hohenberg, P.; Kohn, W. Inhomogeneous Electron Gas. *Phys. Rev.* **1964**, *136*, B864−B871.

(27) Kresse, G.; Joubert, D. From Ultrasoft Pseudopotentials to the Projector Augmented-Wave Method. *Phys. Rev. B: Condens. Matter Mater. Phys.* **1999**, *59*, 1758−1775.

(28) Blöchl, P. E. Projector Augmented-Wave Method. *Phys. Rev. B: Condens. Matter Mater. Phys.* **1994**, *50*, 17953−17979.

(29) Kresse, G.; Hafner, J. Ab initiomolecular dynamics for liquid metals. *Phys. Rev. B: Condens. Matter Mater. Phys.* **1993**, *47*, 558−561.

(30) Kresse, G.; Hafner, J. Ab initiomolecular-dynamics simulation of the liquid-metal-amorphous-semiconductor transition in germanium. *Phys. Rev. B: Condens. Matter Mater. Phys.* **1994**, *49*, 14251−14269.

(31) Kresse, G.; Furthmüller, J. Efficiency of Ab-Initio Total Energy Calculations for Metals and Semiconductors Using a Plane-Wave Basis Set. *Comput. Mater. Sci.* **1996**, *6*, 15−50.

(32) Kresse, G.; Furthmüller, J. Efficient iterative schemes forab initiototal-energy calculations using a plane-wave basis set. *Phys. Rev. B: Condens. Matter Mater. Phys.* **1996**, *54*, 11169−11186.

(33) Perdew, J. P.; Ruzsinszky, A.; Csonka, G. I.; Vydrov, O. A.; Scuseria, G. E.; Constantin, L. A.; Zhou, X.; Burke, K. Restoring the Density-Gradient Expansion for Exchange in Solids and Surfaces. *Phys. Rev. Lett.* **2008**, *100*, 136406.

(34) Dudarev, S. L.; Botton, G. A.; Savrasov, S. Y.; Humphreys, C. J.; Sutton, A. P. Electron-energy-loss spectra and the structural stability of nickel oxide: An LSDA+U study. *Phys. Rev. B: Condens. Matter Mater. Phys.* **1998**, *57*, 1505.

(35) López, S.; Romero, A. H.; Mejía-López, J.; Mazo-Zuluaga, J.; Restrepo, J. Structure and Electronic Properties of Iron Oxide Clusters: A First-Principles Study. *Phys. Rev. B: Condens. Matter Mater. Phys.* **2009**, *80*, 085107.

(36) López-Moreno, S.; Romero, A. H.; Mejía-López, J.; Muñoz, A.; Roshchin, I. V. First-Principles Study of Electronic, Vibrational, Elastic, and Magnetic Properties of FeF_2 as a Function of Pressure. *Phys. Rev. B: Condens. Matter Mater. Phys.* **2012**, *85*, 134110.

(37) Mejía-López, J.; Mazo-Zuluaga, J.; López-Moreno, S.; Muñoz, F.; Duque, L. F.; Romero, A. H. Physical Properties of Quasi-One-Dimensional MgO and Fe_3O -Based Nanostructures. *Phys. Rev. B: Condens. Matter Mater. Phys.* **2014**, *90*, 035411.

(38) Monkhorst, H. J.; Pack, J. D. Special Points for Brillouin-Zone Integrations. *Phys. Rev. B: Condens. Matter Mater. Phys.* **1976**, *13*, 5188−5192.

(39) Parlinski, K. *Computer Code PHONON*: Krakow, Poland, 2010.

(40) Achary, S. N.; Errandonea, D.; Muñoz, A.; Rodríguez-Hernández, P.; Manjón, F. J.; Krishna, P. S. R.; Patwe, S. J.; Grover, V.; Tyagi, A. K. Experimental and Theoretical Investigations on the Polymorphism and Metastability of $BiPO_4$. *Dalton Trans.* **2013**, *42*, 14999−15015.

(41) Mujica, A.; Rubio, A.; Muñoz, A.; Needs, R. J. High-Pressure Phases of Group-IV, III-V, and II-VI Compounds. *Rev. Mod. Phys.* **2003**, *75*, 863.

(42) Rietveld, H. M. A Profile Refinement Method for Nuclear and Magnetic Structures. *J. Appl. Crystallogr.* **1969**, *2*, 65−71.

(43) Errandonea, D.; Manjón, F. J.; Garro, N.; Rodríguez-Hernández, P.; Radescu, S.; Mujica, A.; Muñoz, A.; Tu, C. Y. Combined Raman Scattering and Ab Initio Investigation of Pressure-Induced Structural Phase Transitions in the Scintillator $ZnWO_4$. *Phys. Rev. B: Condens. Matter Mater. Phys.* **2008**, *78*, 054116.

(44) Samanta, S.; Li, Q.; Cheng, B.; Huang, Y.; Pei, C.; Wang, Q.; Ma, Y.; Wang, L. Phase Coexistence and Pressure-Temperature Phase Evolution of VO_2(A) Nanorods Near the Semiconductor-Semiconductor Transition. *Phys. Rev. B: Condens. Matter Mater. Phys.* **2017**, *95*, 045135.

(45) Akahane, K.; Russo, J.; Tanakab, H. A Possible Four-Phase Coexistence in a Single-Component System. *Nat. Commun.* **2016**, *7*, 12599.

(46) Winkler, B.; Milman, V. Density Functional Theory Based Calculations for High Pressure Research. *Z. Kristallogr.* **2014**, *229*, 112−122.

(47) Bandiello, E.; Errandonea, D.; Pellicer-Porres, J.; Garg, A. B.; Rodriguez-Hernandez, P.; Muñoz, A.; Martinez-Garcia, D.; Rao, R.; Popescu, C. Effect of High Pressure on the Crystal Structure and Vibrational Properties of Olivine-Type $LiNiPO_4$. *Inorg. Chem.* **2018**, *57*, 10265−10276.

(48) Errandonea, D.; Meng, Y.; Somayazulu, M.; Häusermann, D. Pressure-induced transition in titanium metal: a systematic study of the effects of uniaxial stress. *Phys. B Condens. Matter* **2005**, *355*, 116−125.

(49) Errandonea, D.; Muñoz, A.; Gonzalez-Platas, J. Comment on "High-Pressure x-Ray Diffraction Study of YBO_3/Eu^{3+}, $GdBO_3$, and $EuBO_3$: Pressure-Induced Amorphization in $GdBO_3$". *J. Appl. Phys.* **2014**, *115*, 216101.

(50) Birch, F. Finite strain isotherm and velocities for single-crystal and polycrystalline NaCl at high pressures and 300°K. *J. Geophys. Res.* **1978**, *83*, 1257−1268.

(51) Angel, R. J.; Gonzalez-Platas, J.; Alvaro, M. EosFit7c and a Fortran Module (Library) for Equation of State Calculations. *Z. Kristallogr.* **2014**, *229*, 405−419.

(52) Hebboul, Z.; Galez, C.; Benbertal, D.; Beauquis, S.; Mugnier, Y.; Benmakhlouf, A.; Bouchenafa, M.; Errandonea, D. Synthesis, Characterization, and Crystal Structure Determination of a New Lithium Zinc Iodate Polymorph $LiZn(IO_3)_3$. *Crystals* **2019**, *9*, 464.

(53) Dove, M. T. Theory of Displacive Phase Transitions in Minerals. *Am. Mineral.* **1997**, *82*, 213−244.

(54) Errandonea, D.; Muñoz, A.; Rodríguez-Hernández, P.; Gomis, O.; Achary, S. N.; Popescu, C.; Patwe, S. J.; Tyagi, A. K. High-Pressure Crystal Structure, Lattice Vibrations, and Band Structure of $BiSbO_4$. *Inorg. Chem.* **2016**, *55*, 4958−4969.

(55) Junaid Bushiri, M.; Kochuthresia, T. C.; Vaidyan, V. K.; Gautier-Luneau, I. Raman Scattering Structural Studies of Nonlinear Optical $M(IO_3)_3$ (M=Fe, Ga, α-In) and Linear Optical β-$In(IO_3)_3$. *J. Nonlinear Opt. Phys. Mater.* **2014**, *23*, 1450039.

(56) Ristić, M.; Musić, S.; Ivanda, M. A Study of the Thermal Stability of $Fe(IO_3)_3$ by ^{57}Fe Mossbauer, FT- IR and Raman Spectroscopies. *J. Mol. Struct.* **1999**, *480−481*, 637−640.

(57) Sun, B.; Dreger, Z. A.; Gupta, Y. M. High-Pressure Effects in Pyrene Crystals: Vibrational Spectroscopy. *J. Phys. Chem. A* **2008**, *112*, 10546−10551.

(58) Errandonea, D.; Pellicer-Porres, J.; Pujol, M. C.; Carvajal, J. J.; Aguiló, M. Room-temperature vibrational properties of potassium gadolinium double tungstate under compression up to 32GPa. *J. Alloys Compd.* **2015**, *638*, 14−20.